PHYSICAL REVIEW A **70**, 033802 (2004)

Competition of multiple filaments during the propagation of intense femtosecond laser pulses

S. A. Hosseini,[1] Q. Luo,[1] B. Ferland,[1] W. Liu,[1] S. L. Chin,[1] O. G. Kosareva,[2] N. A. Panov,[2] N. Aközbek,[3] and V. P. Kandidov[2]
[1]*Centre d'Optique, Photonique et Laser (COPL) et Département de Physique, de Génie Physique et d'Optique, Université Laval, Québec, QC, Canada G1K 7P4*
[2]*International Laser Center, Physics Department, M.V. Lomonosov Moscow State University, Moscow, 119992, Russia*
[3]*Time Domain Corporation, 7057 Old Madison Pike, Huntsville, Alabama 35806, USA*

(Received 8 December 2003; published 7 September 2004)

We observed a universal phenomenon of the competition among multiple filaments generated during the propagation of intense femtosecond laser pulses in air. We show that the fluorescence signal from the excitation of nitrogen molecules inside the plasma channel contains important information pertaining to the formation and interaction of multiple filaments. The detected backscattered nitrogen fluorescence from inside the filaments yielded irregular changes from shot to shot which cannot be explained by fluctuation arising from the initial laser pulse itself. Numerical simulations reveal a complex dynamics of multiple filament propagation and interaction dynamics that depends strongly on the initial perturbations of the laser beam. The irregular changes of the fluorescence signal are attributed to the interference between adjacent hot spots that evolve into filaments which give rise to new hot spots (filaments) in between, and thus give the appearance of the *fusion* or *branching* of filaments.

DOI: 10.1103/PhysRevA.70.033802 PACS number(s): 42.65.Jx, 42.68.Ay, 42.68.Wt, 92.60.Ta

I. INTRODUCTION

The propagation of intense femtosecond near-ir laser pulses in the atmosphere has been the subject of interest both experimentally and theoretically during the last few years due to its potential applications such as atmospheric remote sensing and lightning discharge control [1]. The propagation of intense femtosecond laser pulses in bulk transparent optical media is complicated in general since it involves the strong reshaping of the spatial and temporal profile of the laser pulse through a combined action of linear and nonlinear effects. These effects include group-velocity dispersion (GVD), linear diffraction, self-phase modulation (SPM), self-focusing, multiphoton/tunnel ionization (MPI/TI), plasma defocusing, and self-steepening [2–6]. These processes result in the formation (perception) of a so-called filament with high spatio-temporal localization of the light field and complicated dynamic structure of rings surrounding this localized radiation [7–9]. The filamentation process depends mainly on two competing processes. First, the spatial intensity profile of the laser pulse acts like a focusing lens due to the optical Kerr effect. This causes the beam to self-focus, resulting in an increase of the peak intensity. At high peak intensity, multiphoton ionization of the medium sets in and creates a low-density plasma, causing the beam to defocus. The dynamic balance between self-focusing and plasma defocusing repeats itself, giving the appearance of a stable filament [6]. In the course of filamentation, the pulse self-transforms into a white-light chirped laser pulse known as supercontinuum generation (SCG) [10–12]. The maximum pulse intensity in air is of the order of 5×10^{13} W/cm^2 [13–15]. Under such high peak intensity, atoms and molecules with an ionization potential of up to ~16 eV can be ionized and/or excited through MPI/TI [16–20]. Subsequent collisional electron-ion recombination as well as radiative decay gives rise to a nonlinear fluorescence signal, which for the excited nitrogen molecules and ions N_2^+ is in the range of 300–420 nm [16,21]. Recent observation proved that this fluorescence is amplified along the filament [22].

In a terawatt peak power laser pulse which corresponds to several hundred times the critical power for self-focusing in air, breakup of the laser beam into multiple filaments is unavoidable in practice (see, e.g., Refs. [1,23–25].) The generation of multiple filaments may originate from both laser fluctuations as well as index variations inside the optical medium. Experimental studies on multiple filament formation from two large-scale initial perturbations revealed that at moderate pulse energies (1–5 mJ in 50-fs pulses centered at 800 nm) two hot spots developed from each of the perturbations which subsequently coalesced into one central lobe [26]. At higher input pulse energy (14 mJ in 42-fs pulses centered at 800 nm) each of the two hot spots on the initial beam profile evolved in two interacting filaments [27]. The interaction between the two filaments manifests itself as an interference of transverse ring structures from each filament. The region of the interaction between the filaments was larger if the filamentation started earlier in the propagation. The initial stage of the interaction associated with the development of the perturbations into multiple filaments can be described on the basis of the stationary self-focusing theory [27,28]. However, when the collapse initiated by self-focusing occurs, only nonstationary theory with time-dependent ionization, which stops the collapse, can describe further transformation of the pulse into filaments, etc. In Ref. [29] the evolution of the pulse with initial *regular* modulation across the beam profile was studied in the framework of the (x,y,z,t) propagation model. In most real-life conditions, the initial perturbations on the beam profile and the refractive index of atmospheric air are *irregular*. In a terawatt pulse the starting position of filaments can vary within 10 m due to refractive index fluctuations induced by atmospheric turbulence [30]. Thus, multiple filamentation caused by the random formation of multiple filaments and their subsequent

1050-2947/2004/70(3)/033802(12)/$22.50

interaction is of a random character. As a result, the accompanying plasma (ionization) channel and the associated nonlinear nitrogen fluorescence signal are not stable. The understanding of the fluctuations of the fluorescence signal is essential for femtosecond light detection and ranging (LIDAR) type of applications.

In this work, we study the backscattered fluorescence (BSF) in the propagation of a terawatt Ti-sapphire femtosecond laser pulse for a distance of more than 100 m in air. The BSF signal from multiple filaments produced in the whole range was clearly detectable using a LIDAR system. We found that the backscattered signals varied significantly from shot to shot despite the stable laser pulse energy. Numerical simulations show that this variation is due to the competition among the filaments initiated by the irregular initial perturbations on the beam profile. The scenario of multiple filament competition is very sensitive to the relative location of the initial perturbations. As a result, the plasma channels and the amplified backscattered fluorescence signal strongly depend on the intensity fluctuations in the beam profile and on the relative distance between hot spots.

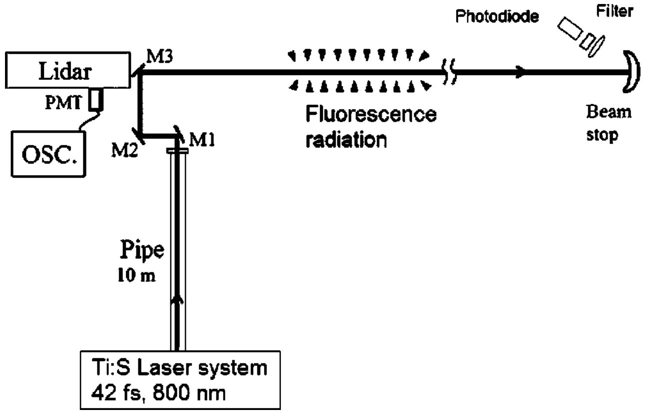

FIG. 1. Schematic diagram of experimental setup; M1, M2, M3 are dielectric mirrors.

II. EXPERIMENTAL SETUP

The versatile multibeam femtosecond laser system used in this experiment was built by Spectra-Physics (SP)/Positive Light. It consists of a regenerative amplifier system (SP, spitfire) based on a Ti:sapphire oscillator (SP, Tsunami, pumped by Millennia). A beam with a repetition rate of 10 Hz is extracted from the 1-KHz output of the regenerative amplifier using a pulse slicer. This beam is sent to a four-pass Ti:sapphire amplifier, pumped by the second harmonic of two Nd:YAG lasers (SP, GCR-350, 10 Hz, 900 mJ/pulse). Finally, the pulse is compressed to 42 fs (FWHM) measured using a single shot auto-correlator (Positive Light SSA). The central wavelength is 800 nm with a bandwidth of 23 nm (FWHM) and a peak power of 2 TW with linear polarization. The pulse is spatially filtered before the four-pass amplifier in order to keep a near-Gaussian spatial distribution. The pulse energy can vary from a few mJ to 85 mJ after the compressor. The beam is then guided to the corridor (length 101 m) through a 10-m vacuum pipe with a 1.5-cm-thick CaF_2 window. The pipe is linked directly to the compressor, which is vacuumed to 10^{-3} Torr. This is to avoid self-focusing in air before the pulse enters the corridor.

The top view of the experiment setup is shown schematically in Fig. 1. The BSF is detected by a PMT (Hamamatsu R7400P, with 1-ns response time; gain$=7\times10^6$) through a LIDAR system. The latter consists of a Newtonian telescope with a spherical mirror (ϕ=16.5 cm) of focal length 90 cm and a small flat mirror (ϕ=3 cm) mounted 10 cm before the focal point of the spherical mirror with 45-deg angle to reflect the collected light onto the PMT mounted at the side. The field of view of the telescope is equal to 20 mrad. Two broadband dielectric mirrors reflecting around 800 ± 25 nm are put in front of the PMT to eliminate any backscattering of the fundamental laser light. Also, a bandpass filter (UG 11, 4 mm thick, passing 200 to 400 nm) is set between the PMT and the 800-nm dielectric mirror. This bandpass filter transmits only the UV region, covering the major spectral lines from nitrogen molecules and ions in the 300–400-nm region.

Strong white-light generation with rainbow-colored rings is observed at the end of the corridor. A photodiode is fixed at the position of 50 cm before the end of the corridor to monitor the occurrence of the white light propagating in the forward direction and, hence, the occurrence of filaments. One 800-nm dielectric mirror and a green filter are used in front of the photodiode to observe a single color of the white light. The PMT and photodiode are connected to a 1-GHz-bandwidth oscilloscope (Tektronix TDS 7254, 2.5-GHz sampling rate) having a 50-Ω input impedance. Another photodiode is put behind one of the reflection mirrors in the TW pump beam path in order to trigger all channels. Since the signals from the first two detectors will arrive with different delay with respect to the trigger channel, a special data acquisition program is developed using LABVIEW software to collect data arising from the same pulse.

III. BACKSCATTERED FLUORESCENCE SIGNAL

For each laser energy, we recorded successive waveforms acquired from the oscilloscope for 300 shots. The experiment was done with different energies of the laser pulse. Figure 2 shows four representative waveforms of the signal for laser pulses with an energy around 40 mJ/pulse. The relative fluctuations of laser energy from shot to shot are within 6% for positive deviation from the average value and 2.5% for the negative deviation. In all panels from (a) to (d) the first peak is due to the scattering of the pump pulse from the last mirror in the setup (M3), and the last peak is from the beam stop that is fixed at the end of the corridor. The middle peaks are due to BSF signals. A close analysis of the BSF signal distributions shown in Fig. 2 demonstrates that the fluorescence signal is very irregular along the filament [Figs. 2(a) and 2(b)]. The irregularity is not the differences in the signal profile but that in certain shots no significant signal is detected at all. When a strong signal is detected it can be seen that it is made up of many peaks along the propagation direction where the amplitude of the peaks decreases in general with propagation distance. The fluorescence yield changes randomly from shot to shot without a correlation with the

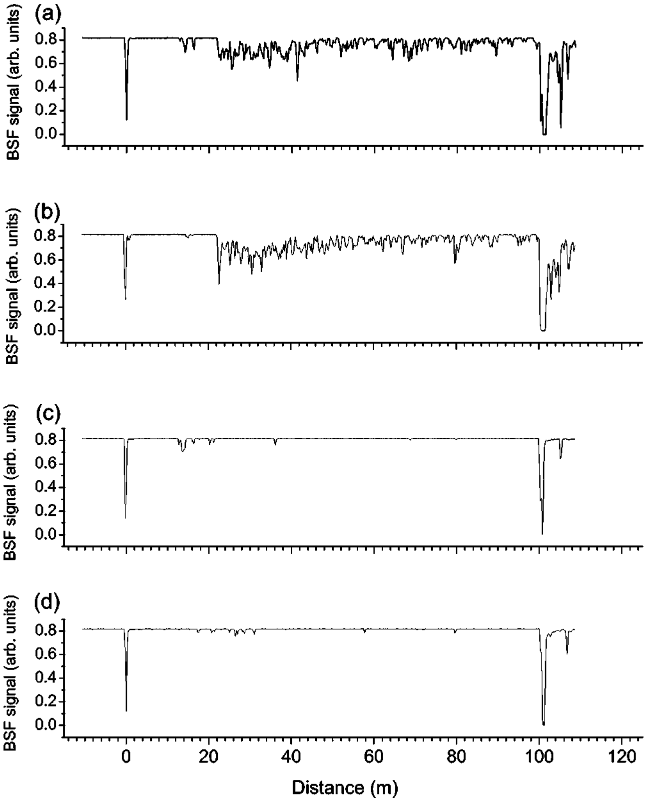

FIG. 2. Four typical BSF signals detected by PMT using a LIDAR technique. The first peak is due to the last mirror in the setup (M3) and the last peak is from the beam stopper that is fixed at the end of the corridor. The middle peaks are BSF signal. The laser energy is (a) 39.4 mJ; (b) 42.4 mJ; (c) 39.4 mJ; (d) 42.4 mJ.

laser energy fluctuations. For example, in Figs. 2(a) and 2(c) the pulse energy is the same, while the signal exists only in the distribution shown in Fig. 2(a). At the same time the increase in energy above the average level of 40 mJ does not necessarily leads to the appearance of the signal [compare Figs. 2(b) and 2(d)].

The physical origin of the irregular fluorescence signal is the following. The variation of the peak intensity and transverse intensity distribution inside the filaments strongly affects the spatial plasma density and its distribution [2,31]. The fluorescence signal originating from the ionization of nitrogen molecules is proportional to the amount of electrons in the plasma. Therefore, there is a close correlation between the plasma density and fluorescence signal. This was shown in our previous work on the feasibility of using the backscattered fluorescence signal to measure the plasma filament length and longitudinal distribution [31]. In the course of multiple filamentation the amount of free electrons in the plasma channels depends on the filament interaction which would lead to the observed fluctuation of the BSF signals.

In Fig. 3 the 3D graph of all 300 shots at 40 mJ/pulse is presented. In this graph the x axis is the direction of propagation of the beam that is calibrated from the time scale of the oscilloscope, and the y axis represents the laser shot number.

In some of the shots, as shown in Figs. 2 and 3, the signal is too weak to be detected. First, we suspected that there was no filamentation and hence, no white-light continuum generation during these shots. However, consistent strong signal from the photodiode at the end of the corridor, as well as the visual observation of the filament burn pattern on paper, indicated that filamentation existed in all the shots. Turbulence in air also could not have explained this strong fluctuation in the signal. Natural refractive index fluctuations, which are typically not larger than 10^{-6}, could not lead to the observed fluorescence signal disappearance.

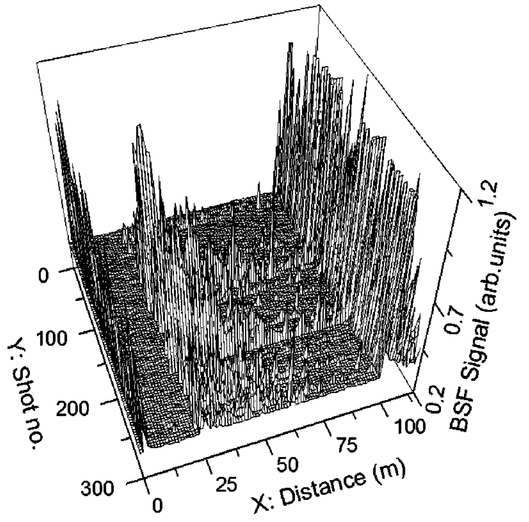

FIG. 3. Three hundred shots of BSF waveform detected by MPT. The laser energy was fixed at 40 mJ/pulse.

Under the current laser pulse parameters, multiple filaments were observed. Figure 4 shows two arbitrary images of the filaments for two different shots with the same input laser energy of 40 mJ 35 m away from the LIDAR system where multiple filaments start to develop. These images are taken by an ordinary digital camera (Canon A40) looking at the surface of a white paper intercepting the beam. The speed of opening of the diaphragm is set at 1/10 s in order to take single-shot images since our laser operates at 10-Hz repetition rate. The image in Fig. 4(a) shows several nearly similar hot spots, each representing a filament. One hot spot is brighter than all the others. In another shot one filament dominates the others [Fig. 4(b)]. A bright halo of conical emission around this filament is the evidence that this dominating filament has been developed earlier than the others in both shots [Figs. 4(a) and 4(b)]. It is important to note that multiple filament formation already started as the pulse passed through the window of the vacuum pipe as shown in Fig. 4(c), which was taken right after the exit window. In our current experimental setup, there was no trivial way yet to avoid the effect of window [25].

IV. NUMERICAL SIMULATIONS

In order to reveal the physical reason for the instability of the fluorescence signal, we performed numerical simulations of multiple filamentation and the formation of plasma channels in the pulse with initial perturbations on the beam profile. Assuming that pulse propagation occurs along the z axis

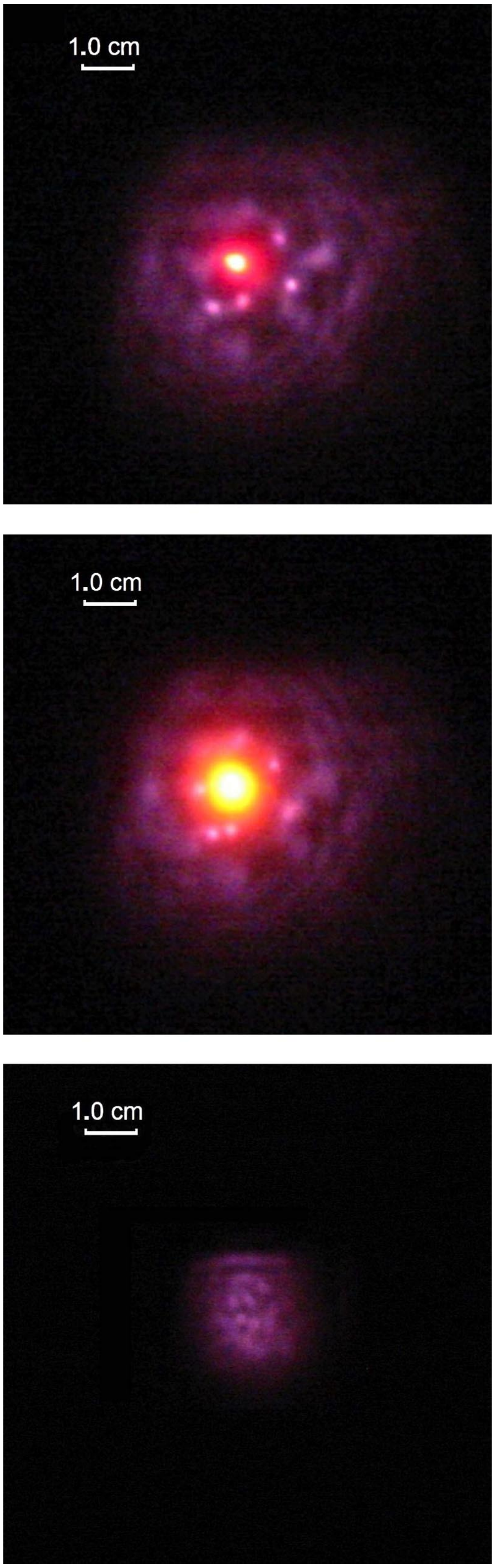

FIG. 4. (a),(b) Two different images obtained from the filament evolution and development at 35 m away from the telescope, where multiple filaments started to develop. (c) Image of the beam, intercepting with a white paper at the exit of the window.

with the group velocity v_g, the equation for the slowly varying amplitude of the electric field $E(x,y,z,t)$ is

$$2ik\left(\frac{\partial E}{\partial z}+\frac{1}{v_g}\frac{\partial E}{\partial t}\right)=\frac{\partial^2 E}{\partial x^2}+\frac{\partial^2 E}{\partial y^2}+\frac{2k^2}{n_0}(\Delta n_k+\Delta n_p)E-ik\alpha E, \tag{1}$$

where the first two terms on the right-hand side of Eq. (1) describe diffraction. In the third term we take into account the nonlinearity of the medium. Following Ref. [27], we represent the Kerr contribution Δn_k in the form $\Delta n_k(t)=n_{2\mathrm{eff}}(t)|E(t)|^2$, where

$$n_{2\,\mathrm{eff}}(t)=\frac{1}{2}n_2\left\{1+|E(t)|^{-2}\int_{-\infty}^{t}H(t-t')|E(t')|^2dt'\right\}. \tag{2}$$

The response function $H(t)$ was defined in Ref. [3]. For the Gaussian pulse with 42-fs duration (at FWHM), $n_{2\mathrm{eff}}(0)=0.57\ n_2$ and the effective critical power for self-focusing $P_{cr\ \mathrm{eff}}=11.8$ GW

The plasma contribution to the refractive index Δn_p is given by

$$\Delta n_p=-\frac{\omega_p^2}{2n_0(\omega^2+\nu_c^2)}\left(1-i\frac{\nu_c}{\omega}\right), \tag{3}$$

where $\omega_p=\sqrt{4\pi e^2N_e/m_e}$ is the plasma frequency, ω is the laser central frequency corresponding to $\lambda=800$ nm, $\nu_c=N_0v_e\sigma_c$ is the effective electron collision frequency with the root-mean-square electron velocity v_e and the electron collision cross section σ_c, N_0 is the density of neutral molecules (20% oxygen and 80% nitrogen).

The free-electron density $N_e(x,y,z,t)$ depends on the spatial coordinates and time according to the kinetic equation

$$\frac{\partial N_e}{\partial t}=R(|E|^2)(N_0-N_e)+\nu_iN_e-\beta N_e^2, \tag{4}$$

where $R(|E|^2)$ is the ionization rate of neutrals and β is the radiative electron recombination coefficient. The avalanche ionization frequency is

$$\nu_i=\frac{1}{W}\frac{e^2E^2}{2m_e(\omega^2+\nu_c^2)}\nu_c, \tag{5}$$

where W is the ionization potential of the air molecules.

In the case of a femtosecond pulse propagation in atmospheric density gases, the effective electron-neutral collision frequency ν_c is much smaller than the laser frequency ω [32], and Eq. (3) for the plasma contribution to the refractive index takes the form

$$\Delta n_p=-\frac{\omega_p^2}{2n_0\omega^2}. \tag{6}$$

In addition, the avalanche ionization frequency ν_i is less than the inverse pulse duration $1/\tau_0$ [32]; therefore, the avalanche does not develop in atmospheric density air. Equation (4) can be rewritten in the form

$$\frac{\partial N_e}{\partial t} = R(|E|^2)(N_0 - N_e), \tag{7}$$

where R is the ionization rates for oxygen and nitrogen molecules.

To calculate the ionization rate $R(|E|^2)$ in Eq. (4) we used the model based on Perelomov, Popov, and Terentev (PPT) [33] for the ionization of a hydrogen-like atom in the linearly polarized electric field E. The values of the effective charges of oxygen and nitrogen molecular ions are taken from Ref. [34] in order to fit the experimental data on ion yields.

The last term on the right-hand side of (1) describes the energy losses due to the ionization, where the absorption coefficient $\alpha = I^{-1} m\hbar\omega(\partial N_e/\partial t)$, m is the order of the multiphoton process, $I = cn_0|E|^2/8\pi$ is the laser pulse intensity, and $k = 2\pi n_0/\lambda$ is a wave number.

For the particular purpose of studying the effect of initial spatial perturbations on multiple filamentation and the formation of plasma channels in condensed medium by the example of water and in atmospheric air, we have neglected the terms associated with self-steepening and material dispersion in Eq. (1). It is shown that these higher-order nonlinear effects mainly influence the temporal dynamics of the pulse as well as the white-light continuum conversion efficiency and, to a lesser extent, the spatial dynamics of the pulse intensity [35]. The shortest duration τ_f of the front part of the pulse after steepening is in the order of 8 fs and 3 fs for water and air, respectively. Therefore, the characteristic dispersion length τ_f^2/k''_ω is 2100 μm and 56 cm, respectively. At the same time, the filament radius a_f in water is approximately 5 μm and in air 40 μm. The corresponding longitudinal scale of spatial transformation ka_f^2 is 190 μm in water and 1.25 cm in air. For both water and air the characteristic scale of spatial transformation ka_f^2 is much shorter than the characteristic scale τ_f^2/k''_ω of the temporal changes. Thus, the spatial effects, which dominate the dynamics of multiple filamentation, develop faster than the temporal effects.

The analysis of single-shot transverse fluence distributions at the CaF_2 window of output of the vacuum system [see Fig. 4(c)] shows the presence of several hot spots formed due to the enhancement of the natural spatial perturbations in this window. In order to understand the effect of the input beam profile on the fluorescence yield, we shall discuss a simpler model with two spatial inhomogeneities in the input beam. This approach opens up the possibility to find out the physical mechanism of the emergence of this instability in the fluorescence signal. To model the inhomogeneities on the beam profile at the laser system output, the initial distribution of the electric field complex amplitude was taken as the sum of the two Gaussian functions

$$E(x,y,z=0,\tau) = e^{-\tau^2/2\tau_0^2} E(x,y),$$

where

$$E(x,y) = E_1 \exp\left[-\frac{(y-y_1)^2 + x^2}{2a_1^2}\right] + E_2 \exp\left[-\frac{(y-y_2)^2 + x^2}{2a_2^2}\right], \tag{8}$$

where $\tau = t - z/v_g$ is the retarded time coordinate, $E_{1,2}$, $(0, y_{1,2})$, $a_{1,2}$ are the amplitude, position, and radius of the first (second) perturbation.

By introducing two deterministic inhomogeneities in the beam profile, we study the effect of one parameter, namely the distance between the perturbation maxima, on the fluorescence signal amplification. Statistical analysis performed on the basis of the actual intensity distribution is a problem with many random parameters such as geometrical positions and transverse size of hot spots, the value of the local fluence maxima, the total pulse energy, etc. All of these values are fluctuating from shot to shot. In order to obtain a quantitative analysis to this stochastic problem it would be necessary to use a Monte Carlo method in the numerical simulation. However, we believe that such a detailed calculation will not reveal the underlying physical mechanism of the observed signal instability. Our main goal in this paper is to provide a simple physical explanation of this phenomenon. As shown below, the model given by Eq. (8) is sufficient to capture the underlying physical mechanism of the fluorescence fluctuation.

The value of $\tau_0 = 25$ fs corresponds to the pulse duration used in the experiment and equal to 42 fs at FWHM. The peak power of the pulse (8) was calculated as

$$P_{\mathrm{peak}} = \frac{cn_0}{8\pi} \int_{-\infty}^{\infty} \int_{-\infty}^{\infty} |E(x,y)|^2 dx\, dy. \tag{9}$$

In the simulations the ratio of the peak power, P_{peak} defined in Eq. (9), to the critical power for self-focusing, $P_{cr\ \mathrm{eff}}$ was varied from 1.5 to 20.

The system of Eqs. (1)–(5) was solved on a grid with nonequidistant grid steps along both x and y coordinates. The size of the grid steps was dependent on the step number and was decreased in the region of inhomogeneities. The overall grid size was (450×450) in the transverse plane and 512 equidistant steps in the time domain. This is the maximum possible size that could be processed on our computer (AMD Athlon™ MP 1900+, 1 GB RAM). The number of z steps varied from 500 to 1000 and was larger for the larger ratio of the pulse peak power to the critical power for self-focusing in the medium. To check the validity of the simulations we tested the phase growth between the current grid point and the neighboring points in the directions (x, y, τ) at each propagation step along the coordinate z. Throughout all the calculations this phase growth did not exceed 0.3 rad.

V. SCENARIO OF THE FILAMENT COMPETITION

Laser pulse filamentation during the propagation of ultrashort high peak power laser pulses is a universal phenomenon that occurs in gases, liquids, and condensed matter. Due to the lower order of multiphoton process in water (5-photon) in comparison with air (8-photon), spatio-temporal gradients of the electric field envelope in water are smaller than in air. This allows us to follow the multiple filamentation process from the beginning, associated with the birth of a first filament, till the end, marked by the survival of the last filament out of the group. Therefore, we first consider water

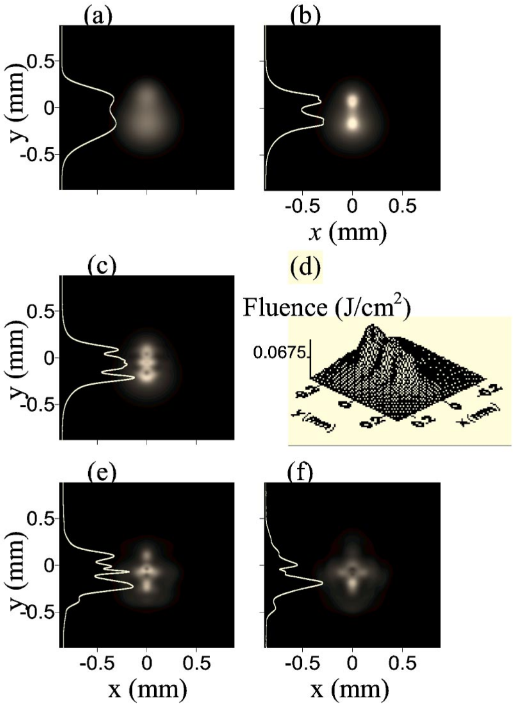

FIG. 5. The transverse fluence distribution demonstrating multiple filament competition in a 42-fs pulse propagating in water for $P_{\mathrm{peak}}/P_{\mathrm{cr}}=4.023$. Initial fluence distribution at $z=0$ (a); the two independently developed parent filaments at $z=0.2z_{\mathrm{d}}$ (b); the birth of the child filament due to the interference $z=0.3z_{\mathrm{d}}$ (c),(d); deterioration of one of the parent filaments at $z=0.45z_{\mathrm{d}}$ (e); survival of one filament at $z=0.55z_{\mathrm{d}}$ (f). The color scale is the same for all plots (a),(b),(c),(e),(f) and the white color corresponds to $0.144\ \mathrm{J/cm^2}$.

as a representative example to study multiple filamentation and the interaction dynamics with relatively lower input powers ($P_{\mathrm{peak}}/P_{\mathrm{cr}}=4.02$). This will allow us to understand the physical mechanism of multiple filamentation and interaction dynamics and its dependence on the initial laser pulse parameters. We will discuss multiple filamentation in air in the next section. In the simulations the Kerr and plasma nonlinearities arising in water were calculated according to Eqs. (3)–(5), where the avalanche ionization is taken into account. The detailed description of all of the constants used in these equations can be found in Ref. [36].

The transverse fluence distribution is a quantity that can be measured in most experiments for femtosecond laser pulse propagation. Therefore, in Fig. 5 [panels (a) to (f)] we represent the scenario of filament competition by plotting the fluence distribution as a function of propagation distance using an initial pulse duration of 42 fs propagating in water. White solid curves show the profile of the fluence distribution along the y axis ($x=0$). Panel (a) shows the beam at the entrance to the medium [see Eq. (8)]. The radius, position, and peak intensity of the larger perturbation are $a_1=0.22$ mm, $y_1=-0.22$ mm, and $I_1=c|E_1|^2n_0/8\pi=1.1\times10^{10}\ \mathrm{W/cm^2}$, respectively, and the same values for the smaller perturbation are $a_2=0.055$ mm, $y_2=0.22$ mm, $I_2=c|E_2|^2n_0/8\pi=4\times10^{9}\ \mathrm{W/cm^2}$. The resulting separation distance between the two maxima of Eq. (8) is $d=1.1a_1$.

The fluence distribution at the laser system output ($z=0$) has two weakly pronounced maxima along the line $x=0$ [Fig. 5(a)]. Up to $z=0.2z_{\mathrm{d}}$, where $z_{\mathrm{d}}=ka_1^2=38$ cm, initial perturbations evolve into two independent developed filaments [Fig. 5(b)]. This is the first stage of the filament competition scenario. By "developed" filament we mean that a perturbation has undergone through the full filamentation processes, namely: GVD, linear diffraction, SPM, self-focusing, MPI/TI, plasma defocusing and self-steepening. The signature of the defocusing is in the rings surrounding any developed filament. The two local minima at the top of the peaks shown in the fluence profile of Fig. 5(b) prove that each of the filaments is developed. With further propagation the radii of transverse rings increase [8] and the two systems of rings start to interfere with each other, since they are part of the same laser pulse and thus are coherent. Starting from $z\approx0.2z_{\mathrm{d}}$ the system of rings diverging from the filament located at ($x=0$, $y_1=-0.22$ mm) interacts with the system of rings diverging from the second filament at ($x=0$, $y_2=0.22$ mm) and creates perturbations within the region $y_1<y<y_2$. By $z=0.3z_{\mathrm{d}}$ the "child" filament born from the interference of the two "parent" filaments is developed in the fluence distribution. In Fig. 5 the fluence distribution at this distance is shown both in black and white color scale [Fig. 5(c)] and as a surface plot [Fig. 5(d)]. The ring at the top of the larger perturbation ($y_1=-0.22$ mm) shows clear asymmetry relative to the filament axis, which is due to the radiation coming from the smaller perturbation ($y_2=0.22$ mm). The child filament located between the two parent filaments is a developed filament itself since it has formed its own plasma column and is surrounded by rings. The indication for this is the slightly pronounced local minimum at the top of the middle peak of the child filament [Fig. 5(d), $y\approx0$]. The formation of the child filament due to the interference of the ring systems produced by initially independent filaments is the second stage of the competition scenario. Here, we note that the interference of the divergent fields of filaments developed earlier in the propagation initiates the formation and defines the position of new filaments.

Further in the propagation the geometrical configuration of the interference pattern of the two parent filaments leads to splitting of the third filament into two by $z=0.45z_{\mathrm{d}}$ [Fig. 5(e)]. However, by this distance the pulse loses ≈20% of its initial energy mainly due to the plasma heating. Therefore, the necessary condition for the development of the fourth mature filament ($P_{\mathrm{peak}}/P_{\mathrm{cr}}\geqslant4$, see, e.g., Ref. [37]) is no longer valid and there is not enough energy to feed four filaments. The result of this competition for energy is the disappearance of one of the parent filaments [see the deterioration of the peak at the position $y=0.2$ mm, $x=0$ in Fig. 5(e)]. Finally, at $z=0.55z_{\mathrm{d}}$ only one filament survives the competition [Fig. 5(f)]. The total energy loss at this distance is not significantly high relative to the initial pulse energy. However, most of the pulse energy is contained in the large background of the beam as only a small percentage of the total energy is channeled into the small core radius [compare the size of the background in Figs. 5(b) and 5(c)]. We note that after a certain propagation distance the number of filaments decreases even without any energy losses. The reason for this is the spatial transformation of the radiation from a

Gaussian or nearly Gaussian to a higher order mode, for which the critical power for self-focusing is larger than that for a Gaussian mode. The decrease of the total number of filaments due to both energy loss and spatial transformation of the radiation and survival of one filament out of the group are the third and the fourth stages of the filament competition scenario, respectively. The decrease of the total number of filaments due to both energy loss and spatial transformation of the radiation is the third stage of the filament competition scenario. Survival of one filament out of the group is the fourth stage of the filament competition scenario.

Thus, the competition of filaments is a complicated dynamical process, which evolves in the direction of the pulse propagation. The competition includes independent development of the parent filaments from the initial perturbations; interference of fields of the parent filaments, which leads to the formation of the new perturbations; the birth of child filaments from these new perturbations; redistribution of the laser energy between all the filaments resulting in the survival of several filaments and disappearance of the others.

VI. FAVORABLE AND UNFAVORABLE CONDITIONS FOR FILAMENT DEVELOPMENT

In the actual experimental conditions the location of inhomogeneities on the beam profile can vary from shot to shot. To model this situation we considered the propagation in air of the two pulses at the same input energy and, hence, the same peak power P_{peak}. The only parameter that was varied was the separation distance d between the initial perturbations, i.e., between the two maxima of the function given by Eq. (8). In the initial pulse distribution (8) the radius of the larger perturbation is $a_1=0.18$ mm and for the smaller perturbation $a_2=0.045$ mm. Their intensities were approximately the same, $I_1=I_2\approx 10^{13}\ \text{W/cm}^2$. We discuss two cases of the relative location of the two perturbations: $y_1=-0.9a_1$, $y_2=0.9a_1$ and $y_1=-0.75a_1$, $y_2=0.75a_1$, respectively. The separation distances between the two maxima of the function (8) are $d_{\text{long}}=1.6a_1=0.29$ mm and $d_{\text{short}}=1.15a_1=0.2$ mm (30% less than d_{long}), respectively [Figs. 6(b) and 6(a)].

The chosen deviation of the distance between the perturbations is close to the one observed in the experiment. Indeed, the analysis of single-shot transverse fluence distributions at the output CaF_2 window [see Fig. 4(c)] shows the presence of several hot spots formed due to the enhancement of the natural perturbations on the beam profile in the window. We have analyzed x and y cross sections of a group of these fluence distributions and found that both cross sections have the two major local maxima. The standard deviation of the distance between the maxima from the mean value is 23%.

In the simulations, the 30% difference in distance between the perturbations corresponds to the largest deviation obtained from the analysis of the experimental data. We have not performed random variation of this parameter with subsequent statistical processing of laser shots since our model describes the actual spatial inhomogeneities only qualitatively.

For the current case of propagation in air, the plasma contribution to the refractive index was considered in the form of Eq. (6) and the growth of electrons was found from Eq. (7). During calculation of ionization rates, we used the values of the effective charges 0.53 and 0.9 for oxygen and nitrogen molecular ions O_2^+, N_2^+, respectively. These values provide the best fit to the experimental data on molecular ion yield [34].

The ratio of the pulse peak power to the critical power for self-focusing was $P_{\text{peak}}/P_{\text{cr}}=11$ and the corresponding input

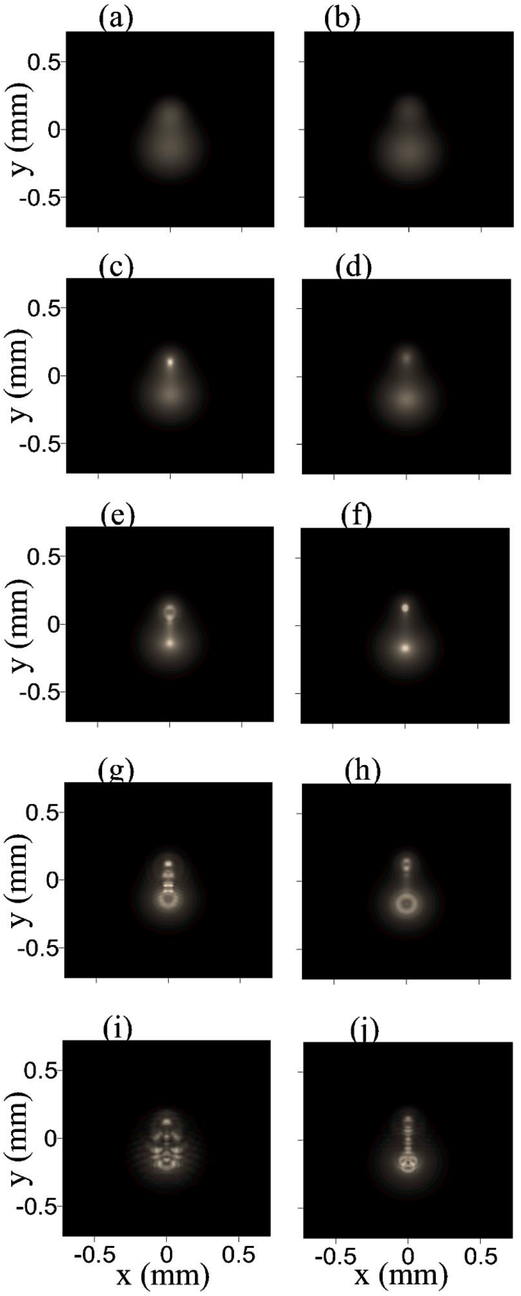

FIG. 6. The transverse fluence distribution for the shorter $d_{\text{short}}=1.15a_1=0.2$ mm (left column) and the longer $d_{\text{long}}=1.6a_1=0.29$ mm (right column) separation distances between the maxima of the initial perturbations in a 42LIfs pulse propagating in air. The ratio $P_{\text{peak}}/P_{\text{cr\_eff}}$ is equal to 11. (a),(b) $z=0$; (c),(d) $z=0.06z_{\text{d}}$; (e),(f) $z=0.08z_{\text{d}}$; (g),(h) $z=0.1z_{\text{d}}$; (i),(j) $z=0.13z_{\text{d}}$. The color scale is the same for all panels (a)–(j) and the white color corresponds to $370\ \text{J/cm}^2$.

pulse energy was 5 mJ. Successive formation of multiple filaments is shown in the fluence distribution (Fig. 6). Panels (a),(c),(e),(g),(i) (left column) in Fig. 6 correspond to the shorter separation distance d_{short} and panels (b),(d),(f),(h),(j) (right column) correspond to the longer distance d_{long}. Larger overlap of the initial perturbations for the case of the shorter separation distance d_{short} leads to the earlier formation of the first parent filament [$z=0.06z_{\mathrm{d}}$ in Fig. 6(c)]. The propagation distance z is scaled by the diffraction length of the first perturbation $z_{\mathrm{d}}=ka_1^2=25$ cm.

In the case of a longer separation distance the two parent filaments are formed nearly simultaneously at $z\approx 0.08z_{\mathrm{d}}$, as shown in Fig. 6(f). The birth of the child filaments occurs earlier in the propagation direction for shorter distance d_{short} than in the case of a longer distance d_{long} [Figs. 6(e) and 6(h)]. In the case of d_{long} the first child filament is born slightly before $z\approx 0.1z_{\mathrm{d}}$. One might notice that the ring structure of the perturbation located at $y\approx -0.2$ mm in Fig. 6(h) is nearly undisturbed and only the edge rings "feel" the second filament and participate in the child formation. Simultaneously, many interference strips are observed at the same distance of $0.1z_{\mathrm{d}}$ for the case of shorter separation distance d_{short} [Fig. 6(g)].

More intense interference results in the larger amount of child filaments in panels (g),(i) in comparison with the panels (h),(j). Moreover, for the farther location of initial perturbations the region of the interference is smaller and the child filaments are mainly located on the line connecting the centers of the two parent filaments [Figs. 6(h) and 6(j)[, while some of the child filaments for the case of closer location of initial perturbations are distributed in the wide region surrounding the parents [Fig. 6(i)]. The latter would mean that some child filaments would be born beside a parent filament but not at a position along the axis between the two parent filaments.

Thus, we can follow the first two stages of filament competition scenario in Fig. 6: formation of independent filaments in panels (c),(d),(f); birth of the first child in panels (e),(h); further formation of child up to at least $z=0.13z_{\mathrm{d}}$ in panels (g),(i),(j).

Temporally resolved dynamics of multiple filament formation for the case of the shorter separation distance d_{short} is shown in Fig. 7, where the equal-intensity contours are plotted in the coordinates (y,τ) and the coordinate x is set to 0. The propagation distance is $z=0.12z_d$. The regions of the contour condensation correspond to the filaments and show their positions in space and time. We can see the formation of at least nine developed filaments at this distance. The two parent filaments at $y=-0.14$ mm and $y=0.08$ mm are formed earlier in the pulse ($\tau\approx -20$ fs and $\tau\approx -24$ fs) and their defocusing rings start to interfere later by $\tau\approx -16$ fs. Within the period -16 fs and till the central slice of the pulse $\tau\approx 0$ fs six child filaments are formed and the seventh child is born later on the intense wing of the parent filament at $\tau\approx 3$ fs.

The evidence for the development of multiple filaments is the presence of the plasma peaks corresponding to each of them (see the left inset in Fig. 7). There is more plasma in the parent filaments in comparison with the child filaments. Different interference patterns in the two cases of larger and shorter separation distances between the maxima of initial perturbations lead to essentially different character of plasma channels. We recall here that the electron density in air is roughly proportional to the eighth power of the pulse's peak intensity. Thus, one might expect that even a slight intensity variation in the interference pattern would lead to a noticeable change in the plasma density and hence, in the fluorescence signal.

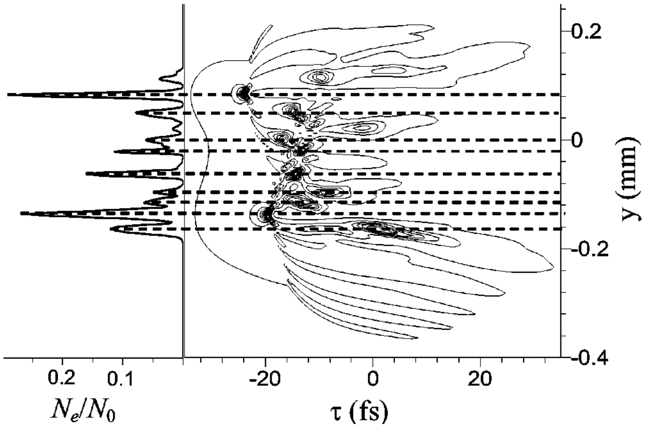

FIG. 7. Equal-intensity contours $I(x=0,y,\tau)$ for the shorter $d_{\mathrm{short}}=1.15a_1=0.2$ mm separation distance between the initial perturbations (right plot) and the corresponding electron density distribution $N_e(x=0,y)$ at the end of the pulse. Propagation distance $z=0.12z_{\mathrm{d}}$. Horizontal dashed lines show the plasma column corresponding to each filament. The contours start from the minimum contour $I_{\mathrm{min}}/I_0=0.7$ and the interval between the contours is $\Delta I/I_0=4.0$, where $I_0=8.6\times 10^{12}$ W/cm^2. N_0 is the density of neutrals before the pulse. Horizontal dashed lines show the plasma peak corresponding to each particular filament.

Maps of the electron density distribution in the plane parallel to the propagation direction $(x=0,y,z)$ are plotted at the end of the pulse in panels (a),(c) of Fig. 8. The panels (b) and (d) show the transverse cross sections of the plasma at $z=0.15z_{\mathrm{d}}$, and panel (e) demonstrates the linear electron density D_{e}, characterizing the total amount of free electrons in the transverse beam section

$$D_e(z)=\int_{-\infty}^{\infty}\int_{-\infty}^{\infty} N_e(x,y,z)dx\,dy, \tag{10}$$

where $N_{\mathrm{e}}(x,y,z)$ is the electron density generated by the end of the pulse.

In panels (a) and (b), corresponding to the shorter separation distance d_{short}, the peaks of the plasma density are higher [see the plasma columns at $y=-0.14$ mm and $y=0.08$ mm in Fig. 8(a)] and there is a larger number of secondary plasma columns in comparison with the case shown in panels (d),(e), especially in the range $0.08z_{\mathrm{d}}$–$0.11z_{\mathrm{d}}$. The case of the shorter distance between the initial perturbations is characterized by the earlier start of the plasma at $z\approx 0.06z_{\mathrm{d}}$ instead of $z\approx 0.08z_{\mathrm{d}}$ [compare Figs. 8(a) and 8(c)]. Thus, the larger amount of free electrons in the beam cross section is obtained at nearly all distances z [Fig. 8(e)].

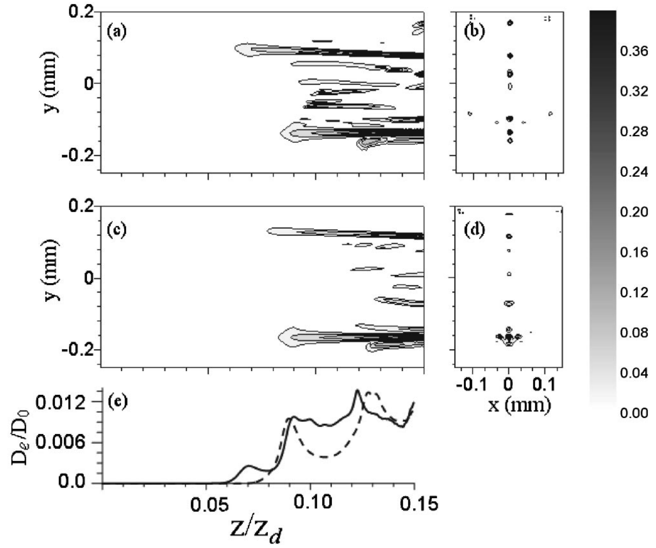

FIG. 8. Electron density distribution for the shorter $d_{\rm short}=1.15a_1=0.2$ mm (a),(b) and the longer $d_{\rm long}=1.6a_1=0.29$ mm (c),(d) separation distances between the maxima of the initial perturbations in a 42 fs pulse propagating in air. The ratio $P_{\rm peak}/P_{\rm cr\_eff}=11$. (a),(c) are the electron density $N_e(x=0,y,z)$ at the end of the pulse. (b),(d) The transverse distribution of the electron density $N_e(x,y)$ at $z=0.15z_{\rm d}$. The interval between the equal-electron-density contours in panels (a)–(d) is $0.05N_0$; the minimum electron density contour corresponds to the same value $0.05N_0$. (e) The linear electron density at the end of the pulse [see Eq. (10)] for shorter (solid curve) and longer (dashed curve) separation distances. The linear density of neutrals D_0 is given by $D_0=N_0a_1^2=8.75\times10^{15}$ cm^{-1}.

VII. SIMULATIONS VERSUS EXPERIMENTAL RESULTS

The fluorescence signal recorded in the experiment depends on the density of plasma and the length of the filament [31]. Qualitatively, it might seem clear that the case of shorter separation distance between the initial perturbation on the beam profile results in larger amplified backscattered fluorescence signal for two reasons: the earlier start of the plasma and the larger number of the secondary plasma columns formed by the child filaments.

The quantitative estimate of the backscattered fluorescence signal $I_{\rm BSF}$ can be done on the basis of the following equation [22], which describes the fluorescence amplification in the plasma:

$$I_{\rm BSF}(x,y,L)=I_{sp}(x,y,l=0)\int_0^L e^{g(x,y,l)l}dl, \tag{11}$$

where the distance l is measured from the end point of our simulations $z=0.15z_{\rm d}$ $(l=0)$ and $l=L$ corresponds to the start of the filament in the case of the shorter separation distance $(z=0.05z_{\rm d})$ between the perturbations. In the absolute units $L=2.5$ cm; therefore, the time of the backscattered signal propagation along this distance (0.08 ns) is less than the lifetime of the population inversion induced by electron-ion recombination (3 ns) and the integration (11) is valid over the whole distance L. For the simple estimate presented here, we did not take into account the diffusion of electrons from the filament region.

Under these assumptions the effective gain coefficient $g(x,y)$ is proportional to the plasma density $N_e(x,y,l)$ and represents both absorption and amplification of the spontaneous emission $I_{\rm sp}$

$$g(x,y,l)=\alpha N_e(x,y,l)\Delta S. \tag{12}$$

In Eq. (12) α is the effective amplification per single electron and $\triangle S$ is a unit area in the transverse beam section.

The effective amplification per single electron α can be estimated from the effective gain coefficient $g=0.3$ cm^{-1} found as a fit to the experimental data in Ref. [22]. In the estimate we assume that the electron density of 10^{16} cm^{-3} is uniformly distributed over the area with the radius of 40 μm [38]. This gives $\alpha\approx6\times10^{-13}$. Substituting this value into Eqs. (11) and (12) and using the simulated plasma density $N_e(x,y,l)$, we calculate the value $I_{\rm BSF}(x,y,L)$ given by Eq. (11). The fluorescence amplified from spontaneous emission of multiple plasma channels is not coherent. Therefore, the backscattered fluorescence signal measured experimentally is proportional to the value $F_{\rm BSF}(x,y,L)$, obtained by integrating $I_{\rm BSF}(x,y,L)$ over the transverse aperture

$$F_{BSF}(l)=\int_{-\infty}^{\infty}\int_{-\infty}^{\infty}I_{BSF}(x,y,l)dx\,dy. \tag{13}$$

The total energy of spontaneous emission in the channel is given by

$$F_{sp}(l=0)=\int_{-\infty}^{\infty}\int_{-\infty}^{\infty}I_{sp}(x,y,l=0)dx\,dy. \tag{14}$$

The calculated results are shown in Fig. 9, where in panel (a) the aperture-integrated fluorescence signal $F_{\rm BSF}$ is plotted as a function of the distance l. In panel (b) the transverse distribution of the fluorescence $I_{\rm BSF}$ is plotted as a function of the coordinate y for fixed $x=0$. The solid curves in both panels (a) and (b) correspond to the shorter separation distance between the initial perturbations, while dashed curves correspond to the longer separation distance. The larger integrated fluorescence signal $F_{\rm BSF}$ is obtained in the case of the closer location of the perturbations [Fig. 9(a)]. This stems from the fact that transverse distribution of fluorescence follows the transverse plasma distribution and it is the strongest at the positions of the most intense plasma columns [compare the plasma density in Fig. 8(a) and the solid curve in Fig. 9(b)]. For the closer location of perturbations the two main peaks at $y\approx-0.14$ mm and $y\approx0.08$ mm are higher due to the larger plasma density. Besides, the contribution of the secondary plasma channels positioned in between the two main peaks $(-0.12\text{ mm}\leqslant y\leqslant0.06\text{ mm})$ is larger than in the case of the longer distance between the perturbations [compare the solid and dashed curves in Fig. 9(b)].

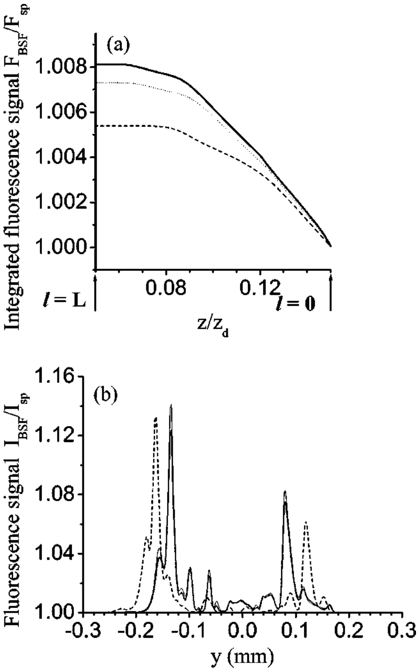

FIG. 9. Fluorescence signal estimated from the simulated plasma density. (a) Integrated over the aperture signal $F_{\mathrm{BSF}}(l)$ [see Eq. (13)]; (b) transverse distribution of the fluorescence $I_{\mathrm{BSF}}(x=0,y,L)$ [see Eq. (11)]. In both panels (a) and (b) solid curve corresponds to the shorter $d_{\mathrm{short}}=1.15a_1=0.2$ mm and dashed curve corresponds to the longer $d_{\mathrm{long}}=1.6a_1=0.29$ mm separation distance between the maxima of the initial perturbations in a 42-fs pulse propagating in air with the ratio $P_{\mathrm{peak}}/P_{\mathrm{cr\_eff}}=11$. In both panels (a) and (b) dotted curve corresponds to the shorter separation distance and 6% of the energy decrease in the initial pulse. In panel (b) dotted curve nearly coincides with the solid curve. The arrows indicate the start $(l=0)$ and the end $(l=L)$ of the fluorescence amplification region.

As shown in the simulations, the two perturbations located 30% closer to each other lead to the earlier start of the plasma and the increase of the linear electron density by up to a factor of 2 at some propagation regions [$z=0.09-0.12z_{\mathrm{d}}$ in Fig. 8(e)]. Electron density increase results in the larger estimated backscattered fluorescence signal (Fig. 9). The scenario of the filament competition is in this case favorable for the formation of a longer and more intense plasma channel and, as a consequence, a stronger fluorescence signal.

To find out the effect of the laser energy fluctuation on the fluorescence signal, we have decreased the energy of the input pulse given by Eq. (8) by 6% for the case of the shorter separation distance between the initial perturbations. The corresponding BSF signal integrated over the transverse aperture closely follows the original signal [compare the solid and dotted lines in Fig. 9(a)] and essentially exceeds the signal for the longer separation distance [compare the dotted and dashed lines in Fig. 9(a)]. The transverse fluorescence distribution I_{BSF} for the case of the decrease of 6% of input pulse energy [dotted line in Fig. 9(b)] can hardly be distinguished from the case without energy decrease [solid curve in Fig. 9(b)]. The difference between the curves is mainly pronounced in the two highest intensity peaks located at $y \approx -0.14$ mm and $y \approx 0.08$ mm. Thus, the change of the separation distance between the perturbations on the beam profile has a much larger effect on the plasma distribution along the filament and the resulting backscattered fluorescence signal than the laser energy fluctuations.

The simulations are in qualitative agreement with the experimental results. Earlier development of filaments and, hence, the plasma channel in some shots in the experiment can be seen in Fig. 4 at a distance of 35 m from the compressor. (The propagation distance of 35 m in the experiment corresponds to $0.05z_{\mathrm{d\_exp}}$, where $z_{\mathrm{d\_exp}}=ka_{0\_\mathrm{exp}^2}=608$ m is the diffraction length of the experimental beam with the radius of $a_{0\_\mathrm{exp}}=0.88$ cm at e^{-1} of intensity level.) Larger radius of the conical emission rings in Fig. 4(b) is evidence of the fact that the source of white light in this shot is located earlier in the propagation than the case shown in Fig. 4(a). Qualitatively, the experimental shot shown in Fig. 4(b) corresponds to the case of the shorter separation distance between the initial perturbations in the simulations, and the shot shown in Fig. 4(a) corresponds to the longer separation distance. The larger halo surrounding the filament in Fig. 4(b) corresponds to the larger radius of the white-light conical emission rings. Since the conical emission angles are similar for any propagation distance [7], larger ring radius indicates that the source of the emission is located earlier in the propagation direction. Thus, we can assume that the filament in Fig. 4(b) started earlier in the propagation than the one in Fig. 4(a). By comparing Fig. 4(b) with Fig. 6(e), one can see that for the case of the shorter separation distance in the simulations the earlier developed filament [Fig. 6(c), $z=0.06z_{\mathrm{d}}$] produces a halo in Fig. 6(e), $z=0.08z_{\mathrm{d}}$. At the same time, for the case of the longer separation distance we see just two hot spots in Fig. 6(f) at the similar distance $z=0.08z_{\mathrm{d}}$. That means in the simulations at the same propagation distance the existence or the lack of the halo depends on the initial separation distance between the perturbations. Hence, for the experimental shots taken at the same distance, the shot with larger halo in Fig. 4(b) corresponds to the case of the closer location of the initial perturbations, while the shot in Fig. 4(b) corresponds to the farther location of the perturbations. Knowing that in the simulations the closer located perturbations (Fig. 6, left column) lead to the stronger fluorescence signal, we might expect that the fluorescence signal in the shot shown in Fig. 4(b) would be larger than in the shot shown in Fig. 4(a).

Thus, random fluctuations of the distance between the hot spots in the experiment lead to either a favorable or unfavorable situation for the plasma channel formation, which generates either strong or weak backscattered fluorescence signal from one laser shot to another as shown in Figs. 2 and 3.

VIII. CONCLUSIONS

In summary, we measured the backscattered fluorescence signal from nitrogen molecules generated from a 42-fs pulse centered at 800 nm with input energies ranging from 20 to 60 mJ/pulse in air. We found that the fluorescence yield exhibits irregular changes from laser shot to shot that cannot be explained by laser fluctuations. Images of multiple filaments observed in the experiment indicate that the filament starting position and development is different for each laser shot. The reason for this is that multiple filament competition follows different scenarios depending on the distance between the perturbations on the beam profile, which changes from laser shot to shot.

In general, the filament competition consists of several stages including independent formation of filaments, the birth of the child filaments from the interference of the ring structures of the initially developed filaments, decrease of the total number of filaments due to both energy loss as well as the spatial transformation of the radiation, and the survival of one filament out of the group.

We have studied the effect of the initial perturbations on the beam profile on the filament competition scenario, formation of plasma channels, and amplification of backscattered fluorescence signal. In the case of the closer separation of the initial perturbations, the interference of the ring structures leads to the formation of a larger number of child filaments and, as a consequence, a more intense and longer plasma channel, which gives rise to a higher fluorescence signal. This conclusion was confirmed in a recent experiment in which the diameter of the same laser pulse was reduced 3.3 times to about 7.5 mm by an inverted telescope. The initial hot spots/filaments were thus closer to one another. Indeed, the BSF signal from the full 100-m range was very stable without any “fluctuation” of the type shown in Figs. 2 and 3. (The details of these results will be reported elsewhere.) In the case of the larger separation distance between the initial perturbations the plasma channel starts later in the propagation and the number of electrons in nearly each cross section is smaller as compared to the closer location of the perturbations. The resulting backscattered fluorescence signal is thus much weaker. The change of the relative position between the perturbations has a larger effect on the plasma density and the fluorescence signal in comparison with the laser energy fluctuations.

Finally, the understanding of the initiations of multiple filaments, consequent propagation, and interaction dynamics is important in the control of random fluctuations of the input laser pulse that may lead to longer propagation distances, which is particularly important for LIDAR applications.

ACKNOWLEDGMENTS

We would like to acknowledge Dr. G. Roy for the design and construction of the LIDAR system. Also, we acknowledge the technical support of M. Martin. This work was supported in part by NSERC, DRDC-Valcartier, Canada Research Chairs, CIPI, FQRNT, and NATO. O.G. Kosareva, N.A. Panov, and V.P. Kandidov are supported by the European Research Office of the U.S. Army under Contract No. N62558-03-M-0029 and the Russian Foundation for Basic Research, Grant N 03-02-16939.

---

[1] J. Kasparian, M. Rodriguez, G. Méjean, J. Yu, E. Salmon, H. Wille, R. Bourayou, S. Frey, Y.-B. André, A. Mysyrowicz, R. Sauerbrey, J.-P. Wolf, and L. Wöste, Science **301**, 61 (2003).

[2] A. Chiron, B. Lamoroux, R. Lange, J.-F. Ripoche, M. Franco, B. Prade, G. Bonnaud, G. Riazuelo, and A. Mysyrowicz, Eur. Phys. J. D **6**, 383 (1999).

[3] M. Mlejnek, E.M. Wright, and J.V. Moloney, Opt. Lett. **23**, 382 (1998)

[4] P. Sprangle, J. R. Penano, and B. Hafizi, Phys. Rev. E **66**, 046418 (2002).

[5] I.S. Golubtsov and O.G. Kosareva, J. Opt. Technol. **69**, 462 (2002).

[6] N. Akozbek, C. M. Bowden, A. Talebpour, and S.L. Chin, Phys. Rev. E **61**, 4540 (2000).

[7] O.G. Kosareva, V.P. Kandidov, A. Brodeur, and S.L. Chin, J. Nonlinear Opt. Phys. Mater. **6**, 485 (1997)

[8] V.P. Kandidov, O.G. Kosareva, and A.A. Koltun, Quantum Electron. **33**, 69 (2003).

[9] S.L. Chin, N. Aközbek, A. Proulx, S. Petit, and C.M. Bowden, Opt. Commun. **188**, 181 (2001) .

[10] S. L. Chin, A. Brodeur, S. Petit, O.G. Kosareva, and V.P. Kandidov, J. Nonlinear Opt. Phys. Mater. **8**, 121 (1999).

[11] N. Akozbek, M. Scalora, C.M. Bowden, and S.L. Chin, Opt. Commun. **191**, 353 (2001).

[12] V.P. Kandidov, O.G. Kosareva, I.S. Golubtsov, W. Liu, A. Becker, N. Akozbek, C.M. Bowden, and S.L. Chin, Appl. Phys. B: Lasers Opt. **77**, 149 (2003).

[13] J. Kasparian, R. Sauerbrey, and S. L. Chin, Appl. Phys. B: Lasers Opt. **71**, 877 (2000).

[14] A. Becker, N. Akozbek, K. Vijayalakshmi, E. Oral, C.M. Bowden, and S.L. Chin, Appl. Phys. B: Lasers Opt. **73**, 287 (2001).

[15] W. Liu, S. Petit, A. Becker, N. Akozbek, C. M. Bowden, and S.L. Chin, Opt. Commun. **202**, 189 (2002).

[16] A. Talebpour, M. Abdel-Fattah, A. D. Bandrauk, and S.L. Chin, Laser Phys. **11**, 68 (2001).

[17] A. Talebpour, A.D. Bandrauk, K. Vijayalakshmi, and S.L. Chin, J. Phys. B **33**, 4615 (2000).

[18] A. Talebpour, K. Vijayalakshmi, A. D. Bandrauk, T. T. Nguyen-Dang, and S.L. Chin, Phys. Rev. A **62**, 042708 (2000).

[19] A. Talebpour, M. Abdel-Fattah, and S.L. Chin, Opt. Commun. **183**, 479 (2000).

[20] A. Becker, A. D. Bandrauk, and S. L. Chin, Chem. Phys. Lett. **343**, 345 (2001).

[21] A. Talebpour, J. Yang, and S. L. Chin, Opt. Commun. **163**, 29 (1999).

[22] Q. Luo, W. Liu, and S. L. Chin, Appl. Phys. B: Lasers Opt. **76**, 337 (2003).

[23] Q. Luo, S.A. Hosseini, B. Ferland, and S.L. Chin, Opt. Commun. **233**, 411 (2004).

[24] H. Schillinger and R. Sauerbrey, Appl. Phys. B: Lasers Opt. **68**, 753 (1999).

[25] W. Liu, S.A. Hosseini, Q. Luo, B. Ferland, S.L. Chin, O.G. Kosareva, N.A. Panov, and V.P. Kandidov, New J. Phys. **6**, 6 (2004).

[26] S. Tzortzakis, L. Berge, A. Couairon, M. Franco, B. Prade, and A. Mysyrowicz, Phys. Rev. Lett. **86**, 5470 (2001).

[27] S.L. Chin, S. Petit, W. Liu, A. Iwasaki, M.-C. Nadeau, V.P. Kandidov, O.G. Kosareva, and K. Yu. Andrianov, Opt. Commun. **210**, 329 (2002).

[28] L. Bergé, M.R. Schmidt, J. Juul Rasmussen, P. L. Christiansen, and K. O. Rasmussen, J. Opt. Soc. Am. B **14**, 2550 (1997).

[29] M. Mlejnek, M. Kolesik, J. V. Moloney, and E.M. Wright, Phys. Rev. Lett. **83**, 2938 (1999).

[30] V.P. Kandidov, O.G. Kosareva, M.P. Tamarov, A. Brodeur, and S.L. Chin, Quantum Electron. **29**, 911 (1999).

[31] A. Iwasaki, N. Aközbek, B. Ferland, Q. Luo, G. Roy, C.M. Bowden, and S.L. Chin, Appl. Phys. B: Lasers Opt. **76**, 231 (2003).

[32] V.P. Kandidov, O.G. Kosareva, and S.A. Shlyonov, Quantum Electron. **24**, 905 (1994).

[33] A.M. Perelomov, V.S. Popov, and M.V. Terent'ev, Sov. Phys. JETP **23**, 924 (1966).

[34] A. Talebpour, J. Yang, and S.L. Chin, Opt. Commun. **163**, 29 (1999).

[35] N. Akozbek, M. Scalora, C.M. Bowden, and S.L. Chin, Opt. Commun. **191**, 353 (2001).

[36] W. Liu, O. Kosareva, I.S. Golubtsov, A. Iwasaki, A. Becker, V.P. Kandidov, and S.L. Chin, Appl. Phys. B: Lasers Opt. **76**, 215 (2003).

[37] J. H. Marburger, Prog. Quantum Electron. **4**, 35 (1975).

[38] S. Tzortzakis, M. A. Franco, Y.-B. André, A. Chiron, B. Lamouroux, B. S. Prade, and A. Mysyrowicz, Phys. Rev. E **60**, R3505 (1999).